Interatomic potential for sodium and chlorine in both neutral and ionic states

Hao Sun,[1] Christopher Maxwell,[2] Edmanuel Torres,[2] and Laurent Karim Béland[1,*]
[1]*Department of Mechanical & Materials Engineering, Queen's University, 60 Union Street, Kingston, Ontario, Canada*
[2]*Canadian Nuclear Laboratories, Chalk River Laboratories, Chalk River, Ontario K0J1J0, Canada*

(Received 8 November 2023; revised 22 April 2024; accepted 24 April 2024; published 17 May 2024)

Molten salts could play an important role in energy storage, in the form of liquid batteries, and heat storage for solar and nuclear power. However, their widespread application is hindered by a limited understanding of the mechanisms by which they corrode metallic containers. This knowledge gap necessitates atomic-scale studies on salt-metal interactions. Molecular dynamics simulations are well suited for such research but require interatomic potential capable of accurately modeling both ionic and neutral states of salt and metal elements. Herein, we developed a moment tensor potential (MTP) with this capability, employing a small-cell training approach. The proposed MTP is compact: It is described by 449 parameters fitted on 609 configurations; 30% of these are one- or two-atom configurations. Extensive testing of our MTP points to a high-fidelity description of the structural and transport properties of solid/liquid Na, gaseous Cl, and crystalline/molten NaCl. Furthermore, we applied this MTP to calculate the standard reduction potential and solubility limit of Na in molten NaCl, achieving results that closely align with experimental and *ab initio* simulation data. This approach offers a robust framework for exploring the electrochemical and physical properties of molten salts across various compositions and solutes.

DOI: 10.1103/PhysRevB.109.174113

I. INTRODUCTION

Molten chloride salts are promising heat transfer mediums for carbon-free energy generation [1,2] and electrolytes of liquid metal/molten salt batteries [3], but their propensity to severely corrode metallic containers limits their application [4,5]. One notable corrosion mechanism is metal dissolution from salt-exposed components to the melt [6]. The dissolved metal also causes self-discharge currents, lowering the efficiency of liquid metal/molten salt batteries [3] and metal production [7,8] by molten salt electrolysis [9]. The solubility limit and corrosion rates of metals in molten salts are linked to the viscosities, self-diffusion coefficients, and heat conductivities of these salts and the standard reduction potential of the metallic atoms in the melt [9]. These properties are challenging to measure experimentally and very demanding to estimate using *ab initio* calculations. Molecular dynamics (MD) simulation is well-suited for such inquiries, yet its accuracy is contingent upon the interatomic potential (IP) employed. Hence, developing IPs for MD simulations of molten salts has become an increasingly important research field.

Currently, multiple semiempirical IPs such as rigid ion models [10] and polarizable ion models [11] can describe multiple structural and dynamic properties of molten salts, but they cannot capture the variations of charge states [12]. Charge transfers can be captured by variable-charge IPs such as ReaxFF [13,14] and COMB [15,16]. However, these IPs have rigid functional forms, which require the inclusion of extra physically motivated terms for specific scenarios [17–19]. Thus, systematically extending the number of parameters of these variable-charge IPs to approximate *ab initio* interactions is challenging. Alternatively, machine-learning IPs offer flexible, functional forms that can be systematically improved. Approaches such as Gaussian approximation potentials (GAPs) [20–22] and neural network IPs (NNIP) [23–32] have been successfully used to model various molten salts. NNIPs have also been proven to capture atomic charge transfer in an organic molecule [33] and multiple charge states of ions in molten salts [34,35]. Nonetheless, MD simulations of metal dissolution and corrosion in molten salts require an IP that can jointly describe metal and its corresponding salts in both solid and liquid phases, neutral and ionic states. To our knowledge, no existing IP fulfills this requirement.

In this paper, as a proof of concept, we employ the moment tensor potential (MTP) [36,37] framework to develop a force field for Na (in solid and liquid phase), Cl (in gaseous phase), and NaCl (in solid and liquid phase). We then validate our MTP by comparing its predictions on multiple structural, thermophysical, and transport properties with those obtained by *ab initio* calculations. Since our MTP was developed to describe both liquid Na and molten NaCl, we investigated the transition of Na from the neutral state in liquid Na to the ionic state in molten NaCl, calculating the standard reduction potential and the solubility limit of Na in molten NaCl. We expect that our method can be generalized to determine the relative position of electrochemical reactions and the electrochemical series for any molten salt solvent.

II. METHODS

A. Machine-learning IP

The MTP framework represents atomic energy $V(n_i)$ as a linear combination of basis functions B_α [36]:

$$V(n_i) = \sum_\alpha \varepsilon_{\alpha(u,v)} B_{\alpha(u,v)}(n_i), \tag{1}$$

*laurent.beland@queensu.ca

where ε_α are fitting parameters. The basis function B_α can be defined by the moment tensor M_α:

$$M_{\alpha(u,v)}(n_i) = \sum_j f_u(|r_{ij}|, n_i, n_j) r_{ij} \otimes \ldots \otimes r_{ij}, \qquad (2)$$

where r_{ij} is the position vector from the atom n_i to n_j. The order parameter α is determined by u and v: f_u represents the sum of Chebyshev polynomials up to an order of u, and v indicates the outer product of r_{ij} by v times. The resulting tensor $M_{\alpha(u,v)}$ is then contracted to a numeric value B_α. Based on a series of B_α, linear regression is applied to minimize the error with respect to energies, forces, and stresses calculated using density functional theory (DFT). We utilized the MLIP-3 package [38] to train our molten salt MTP. In this paper, the energy, force, and stress data points are assigned weights of 100:1:0.01, like in previous MTP works [39–43].

In MTP, the inner and outer cutoff radii determine the maximum and minimum interaction range between atoms. We chose an inner cutoff of 1.85Å for our potential, as the radial distribution functions (RDFs) of liquid Na and molten NaCl in Fig. 1 show that no interatomic distances are <1.85Å. We chose an outer cutoff distance of 8Å. These inner and outer cutoff distances have been used in several machine-learning force fields for molten salts [31,35,44]. The determination of the functional form of MTP, i.e., the number of fitting parameters, can be found in the Supplemental Material [45].

We also constructed a validation set to test the performance of our MTP. The composition of training and validation datasets are listed in Tables SI and SII in the Supplemental Material [45]. Different from the training set, the validation set contains cubic cells having three or four Na atoms, two Na and Cl atoms, or three Na and Cl atoms. All atoms are distributed randomly inside the cell. These structures are thermodynamically unstable, resembling neither solid nor liquid structures. We chose them to ensure that the validation dataset is independent of the training dataset, so they give an unbiased evaluation of the MTP fit on the training dataset with increasing parameters.

B. *Ab initio* quantum mechanical calculations

All configurations in our training, testing, and validation datasets were generated using the QUANTUM ESPRESSO software package [46] and the generalized gradient approximation following Perdew, Burke, and Ernzerhof [47]. Because ionic crystals have neither free electron as in metals nor shared electrons as in covalent bonds, each electron in ionic crystals is bonded to an ion, akin to electrons in isolated atoms. Hence, we chose a semilocal pseudopotential [48] that utilizes spherical-harmonic functions for the nonlocal term in angular coordinates, the same descriptors used for atomic electron wave functions. The kinetic energy cutoff for wave functions was set to be 680 eV, consistent with previous work on the machine-learning potential of molten NaCl [32].

Previous research [49] has found that, without van der Waals corrections, *ab initio* MD (AIMD) simulations of molten NaCl structures can expand indefinitely. This suggests that van der Waals forces are significant to the cohesion of molten salts. Even though Coulombic forces are the dominant forces at short ranges, at longer ranges, the average repulsion between like charges balances the attraction between opposite charges. Based on these earlier studies, we added to our DFT calculations van der Waals corrections with the DFT-D2 scheme of Grimme [50], which has been demonstrated to successfully reproduce the microscopic structure and thermodynamic properties of molten NaCl [49]. We also applied the same correction to all Na and Cl_2 configurations. For all DFT calculations, the convergence criterion for electronic self-consistent calculations is 0.01 meV. Since models of different sizes require different k-point densities for DFT calculations, we tested the energy and force convergence of different models to assess if different k-point densities are an issue (see the Supplemental Material [45] for more details).

All training configurations regarding Cl_2 gas contain a single Cl_2 molecule with varying interatomic distances in a large cell ($15 \times 15 \times 15$Å), so the molecule is not subject to noticeable intermolecular interactions. Because our MTP was trained by models of an isolated Cl_2 molecule, it did not consider any interactions between molecules. Increasing the k-point density to $2 \times 2 \times 2$ only decreased the atomic energy by 0.2 meV/atom and the atomic force by 0.6 meV/Å. Thus, a single k point is enough for both energy and force convergence.

AIMD simulations were carried out at constant volumes and temperatures; the temperature was controlled by a Berendsen thermostat [51] with a time scale of 1 fs. When running AIMD simulations, we used models containing 128 atoms for molten NaCl, and 43 and 117 atoms for liquid Na. The sizes of the 128- and 117-atom models are two times larger than our MTP cutoff distance, so we do not expect an atom in them to see its replica or the same particle twice. Our AIMD obtained the same RDF and diffusion coefficients of molten NaCl as previous work based on a 64-atom model [31]. The 43-atom model of liquid Na also yields the same RDF as that based on the larger 117-atom model and a 64-atom model [49].

C. MTP-MD simulations and active learning algorithms

The trained MTP was used in LAMMPS via an interface with MTP [36]. The system size and simulation temperatures were chosen to be the same as that in AIMD, with a time step of 1 fs. NVT simulations were performed using the Nosé-Hoover thermostat [52] while maintaining periodic boundary conditions. The equilibrated trajectory after 500-ps simulations was used to perform coordination and structure analysis. For the calculation of self-diffusion coefficients, we used the Berendsen thermostat [51] to be consistent with our AIMD simulations.

In the active learning method, n configurations are initially generated and converted to an $n \times m$ matrix (m is the number of the basis MTP functions). MTP then selects m configurations into an active set $\mathbf{A}$ with the maximum modulus of the determinant $|\det(\mathbf{A})|$. This determinant can be viewed as the volume occupied by the active set $\mathbf{A}$ in configurational space (projecting the atomic coordinates on the current MTP basis set). Later, when encountering a new configuration, the program will calculate whether it can increase $|\det(\mathbf{A})|$ by replacing one existing configuration in $\mathbf{A}$. A configuration will be selected for training (flagged risky) only if it can increase

$|\det(\mathbf{A})|$ by a factor >2. Otherwise, the extrapolation error is usually not significantly higher than that for interpolation [36]. Every time the training set is updated, so is the active set. However, if a configuration increases $|\det(\mathbf{A})|$ higher than the maximum allowed extrapolation grade (typically 10 for our calculation [36]), the simulation will be unstable and must be terminated. We must update the active/training set and retrain the potential.

Overall, one iteration of our active learning algorithm consists of the following steps:

(1) A set of n training configurations is generated and converted to an $n \times m$ matrix.

(2) Select from the training dataset m configurations to form an active set $\mathbf{A}$ with the maximum $|\det(\mathbf{A})|$.

(3) Run the simulation with the current potential and the active set until its successful completion or break due to configurations exceeding the maximum allowed extrapolation grade. New training configurations are selected automatically during the simulation.

(4) The *ab initio* calculated energy, forces, and stresses of the selected configurations are appended to the trained set, and the active set is updated to maximize $|\det(\mathbf{A})|$.

(5) The MTP is retrained.

The above iteration repeats until the simulation completes successfully with no risky configurations identified. Using an MTP trained by solid Na and NaCl configurations, we found the first iteration will always break for configurations of liquid structures, yet the second will not. Two iterations are enough for MTP to pick up all risky configurations.

All training configurations are selected based on the active learning algorithm discussed above. For each type of configuration, we created 31 deformed models with volumetric strains evenly distributed from −15 to 15% and then ran an active-learning MTP-MD simulation for each model under the NVT condition. The liquid models are sampled from primary liquid structures predicted by an MTP trained only by solid configurations. To detect risky configurations caused by thermal fluctuations, we ran MTP-MD simulations using the Langevin thermostat [53] at 100, 673, 1273, and 1473 K for solid configurations. Each simulation ran for 1 ns. For liquid structures, training configurations were selected at temperatures beyond the melting points: 373, 673, 973, and 1073 K for liquid Na and 1073, 1273, 1473, and 1555 K for molten NaCl.

D. Performance and cost assessment of MTP

A comprehensive performance and cost assessment of various machine-learning IPs, including MTP and NNIP, can be found in Refs. [42,54]. These comparisons found a tradeoff between accuracy and the number of parameters and, consequently, the computational cost. Compared with NNIP, MTP exhibits an excellent balance between model accuracy and computational efficiency [42]. However, the outcome of such assessments depends heavily on the choice of training and validation datasets and, therefore, on the specifications set by the scientist training the models. Nonetheless, potentials involving more parameters are generally more accurate yet less computationally efficient. We also found the computational cost of MTP [$\sim 10^{-7}$ (CPU h) atom^{-1} (MDstep)$^{-1}$] is 10 times smaller than that of an NNIP for molten NaCl (between 10^{-6} and 10^{-5} (CPU h) atom^{-1} (MDstep)$^{-1}$, as reported in Ref. [31]), close to the cost of the Fumi-Tosi empirical potential [55] (see the Supplemental Material [45] for the figure of performance and cost assessment of MTP).

III. RESULTS

A. Active-learning small-cell strategy for training dataset construction

We adapted a systematic small-cell active-learning strategy previously used to develop MTPs for Zr and Zr hydrides to construct our training set [56,57]. Our small-cell strategy was inspired by the fact that, because DFT provides only the total energy of the whole model under consideration, the MTP optimizer faces a degeneracy when decomposing the total energy into atomic energies. Only 1 or 2 atom cells with identical elements have unambiguous atomic energy partition. Therefore, to alleviate the degeneracy problem, we built an initial training set using multiple 0 K primitive cells of Na and NaCl with volumetric strains from −15 to 15%. Then we expanded our training set via MTP-MD simulations, leveraging the active-learning mode of the MLIP-3 software package [58]. Specifically, we ran active-learning MTP-MD on each deformed NaCl primitive cell at four different temperatures (100, 673, 1273, and 1473 K). Thermally induced atomic vibrations can access microstates different from the 0-K volumetrically deformed structures. During the simulation, the active-learning MTP algorithm automatically selected configurations with interatomic environments distinct from the initial training set. Afterward, we performed DFT calculations on these selected configurations, added the results to the training set, and retrained the MTP. Using this updated MTP, we repeated the active-learning process. Every time new training configurations were identified, the MTP was updated. Finally, no deformed NaCl primitive cells were flagged by the active-learning MD. The same procedure was utilized to introduce into training configurations of Na and NaCl unit cells, molten Na and NaCl models, and Cl_2 gas models.

We constructed a training set containing 609 configurations: 15 Cl_2 molecule models, 339 primitive and unit cells of Na and NaCl, and 74 liquid models with a maximum of 34 atoms. By gradually replacing the Cl atom with Na in such 34-atom configurations, we also included models of supersaturated Na solutions in molten NaCl. Specifically, our training dataset contains only 8 liquid Na configurations, for MTP can infer most of the properties of liquid Na from molten NaCl due to their similarities: the incomplete free electron screening in liquid Na results in an oscillatory ion-ion interaction (the Friedel oscillations) and RDF like that in molten NaCl caused by the excluded-volume effect of the Cl ions; additionally, both Cl ions and free electrons carry the same charge, thereby inducing a similar polarization effect on Na ions at the same distance. Validation using a separate dataset indicated that a relatively modest 449 MTP parameters were sufficient to adequately describe the chemical and physical properties of NaCl, Cl_2 gas, and Na (see discussions in Sec. III B). In contrast,

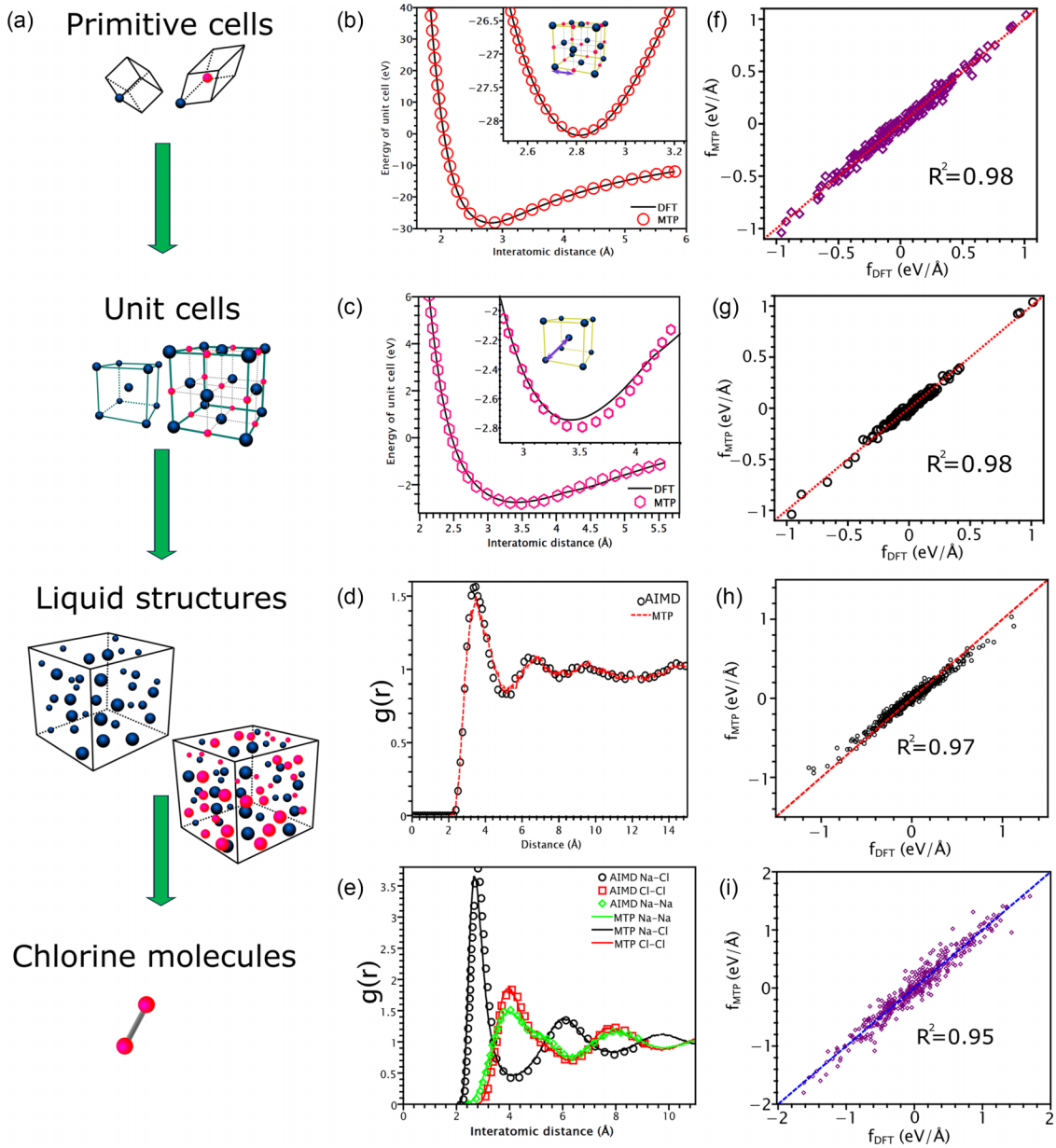

FIG. 1. Machine-learning interatomic-potential development and evaluation. (a) The hierarchical construction of our training dataset. Blue and red atoms represent Na and Cl, respectively. 0 K equations of state for (b) solid NaCl and (c) solid Na. Radial distribution functions of liquid Na and molten NaCl at 1150 K are shown in (d) and (e), respectively. The comparison of moment tensor potential (MTP) atomic force prediction with density functional theory (DFT) results for (f) a 54 atom solid Na model, (g) a 64 atom crystalline NaCl model, (h) a 117 atom liquid Na model, and (i) a 128 atom molten NaCl model.

NNIPs have thousands of parameters [23–32] and thus must use an augmented training dataset (∼10 000 configurations) to alleviate overfitting; GAPs [20–22] also require thousands of molten salt training configurations, each having hundreds of atoms. Our training strategy indicates that such a vast training dataset and large training models are not required. Once trained with the 609 small-cell configurations, the MTP does not flag risk for liquid models containing >34 atoms during further active learning. The information in these large liquid models can be interpolated from crystalline salt and small-cell liquid models. Hence, our semisupervised, small-cell approach has the advantage of being computationally efficient, while minimizing human intervention.

B. MTP predictions on structure properties

Figures 1(b) and 1(c) show the MTP-predicted 0 K equations of the state obtained from the volumetric deformation of the unit cells of NaCl and Na, respectively. They are in very good agreement with DFT calculations, accurately reproducing bulk moduli, cohesive energies, and lattice parameters of both Na and NaCl. Such accuracy is expected because these configurations are included in the training set. To validate that our MTP can capture various interatomic interactions in larger models, we also compared the atomic forces predicted by MTPs and that by AIMD of a 2 × 2 × 2 NaCl supercell model at 850 K [Fig. 1(f)] and a 3 × 3 × 3 Na supercell cell at 300 K

TABLE I. Properties of Na and NaCl, calculated using MTP and DFT. The vacancy formation energy of NaCl is the energy cost for a Na-Cl vacancy pair. Bulk moduli are derived from fitting to the Birch-Murnaghan equation of state, like previous experimental works on NaCl. Due to the addition of dispersion corrections, our DFT-calculated Na properties deviate from experimental observations.

	NaCl			Na		
	DFT	MTP	Experiment	DFT	MTP	Experiment
Cohesive energy (eV)	7.05	7.07	6.62 [59]	1.37	1.4	1.113 [60]
Lattice parameter (Å)	5.62	5.6	5.64 [61]	3.97	4	4.28 [62]
Bulk modulus (GPa)	27	30.8	24 [63]	7.45	8.55	6.3 [64]
Vacancy formation energy (eV)	2.12	2.43	2.12 [65]	0.56	0.35	0.39 [66]
Antisite formation energy (eV)	4.28	4.53				
Simple cubic Na cohesive energy (eV)				1.26	1.27	
Simple cubic Na lattice parameter (Å)				3.19	3.23	
Face-centered cubic Na cohesive energy (eV)				1.36	1.4	
Face-centered cubic Na lattice parameter (Å)				5	5.12	

[Fig. 1(g)]. For both structures, the MTP-predicted forces follow a linear relation with the DFT results with a unity slope. The root mean square errors are 0.025 and 0.042eV/Å for solid Na and crystalline NaCl, respectively. Furthermore, our MTP can also correctly predict the formation energy of defect structures not included in the training set, such as a Na-Cl vacancy pair in NaCl (DFT: 2.12 eV; MTP: 2.43 eV), a NaCl antisite defect (DFT: 4.28 eV; MTP: 4.53 eV), as well as the unstable face-centered cubic (fcc) and simple cubic (sc) structures of Na (Table I). Likewise, with no phonon data included during training, our MTP leads to reasonable NaCl and Na phonon band structures and density of states (see the Supplemental Material [45]).

Next, we compare the structures of molten NaCl and liquid Na obtained via AIMD with those obtained using MTP-MD. Both AIMD and MTP-MD were performed under the isothermal-isovolumetric condition (NVT) at 1150 K with densities of 0.98 and 1.64g/cm^3 for liquid Na and molten NaCl. These are equilibrium densities predicted by our MTP at 1150 K; the density of molten NaCl, 1.64g/cm^3, is slightly higher than the experimental value (1.53g/cm^3 [67]) but consistent with a previous NNIP prediction [31]. Next, we computed the RDF of liquid Na in Fig. 1(d) and the RDFs for the three atomic pairs (Na-Na, Na-Cl, and Cl-Cl) of molten NaCl in Fig. 1(e). MTP-based RDFs of both liquid Na and molten NaCl closely overlap those obtained using *ab initio* calculations. Compared with the experimental RDFs deduced from neutron diffraction measurement [68,69], both AIMD and MTP predict the first and second peak positions and the long-range fluctuations accurately. Our AIMD predicts a shoulder of the Cl-Cl and Na-Na RDFs at 5.3 Å, a structure not observed in experiments. This structure reflects an exaggerated attraction caused by the DFT-D2 dispersion correction [70]. Except for these differences, the microscopic structure of the simulated molten NaCl agrees with that measured experimentally, so the phenomenological behavior of molten NaCl would remain the same with experiments (see the Supplemental Material [45] for more details).

In addition to RDF, our MTP reproduces the angular distribution functions in molten NaCl and liquid Na (see the Supplemental Material [45]). We also compared the atomic forces predicted by MTP with AIMD simulations of 117-atom liquid Na [Fig. 1(h)] and 128-atom molten NaCl [Fig. 1(i)] models at 1150 K. For both liquid structures, the atomic forces predicted by MTP are in line with the DFT results with a unity slope. The root mean square errors are 0.043 and 0.138eV/Å for liquid Na and molten NaCl, respectively. In addition, our MTP predicts a melting point of NaCl consistent with a recently developed NNIP on molten NaCl [31]. These validations of the MTP based on models larger than training configurations indicate that the MTP can capture both the metallic bonding in Na and ionic bonding in NaCl accurately.

Finally, our MTP successfully reproduces the DFT-determined bond-length-bond-energy relationship of Cl_2 gas molecules (see Fig. 2), yielding the same equilibrium bond lengths, bond stiffness, and bond energy as DFT calculations. We further calculated the equation of state for Cl_2 gas at 1150 K using 200 Cl_2 gas molecules. The pressure was averaged over 10-ns NVT simulations at different volumes occupied by these Cl_2 molecules. These molecules remain

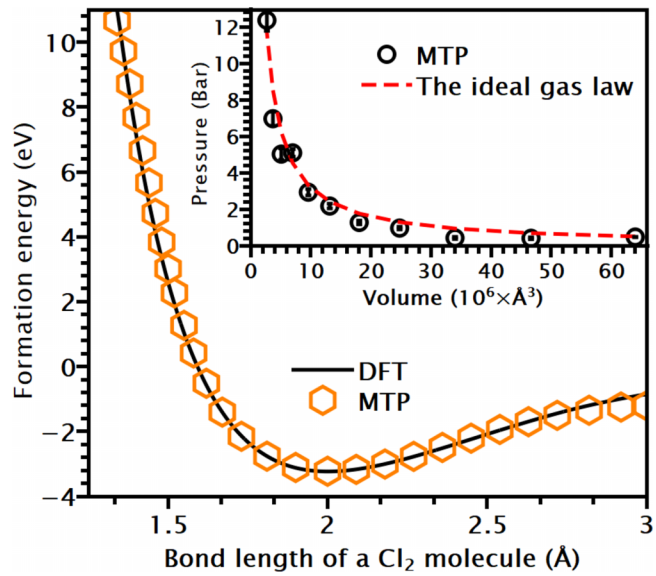

FIG. 2. The bond-length-bond-energy relationship for a Cl gas molecule at 0 K. We also illustrated the equation of state for Cl_2 gas at 1150 K.

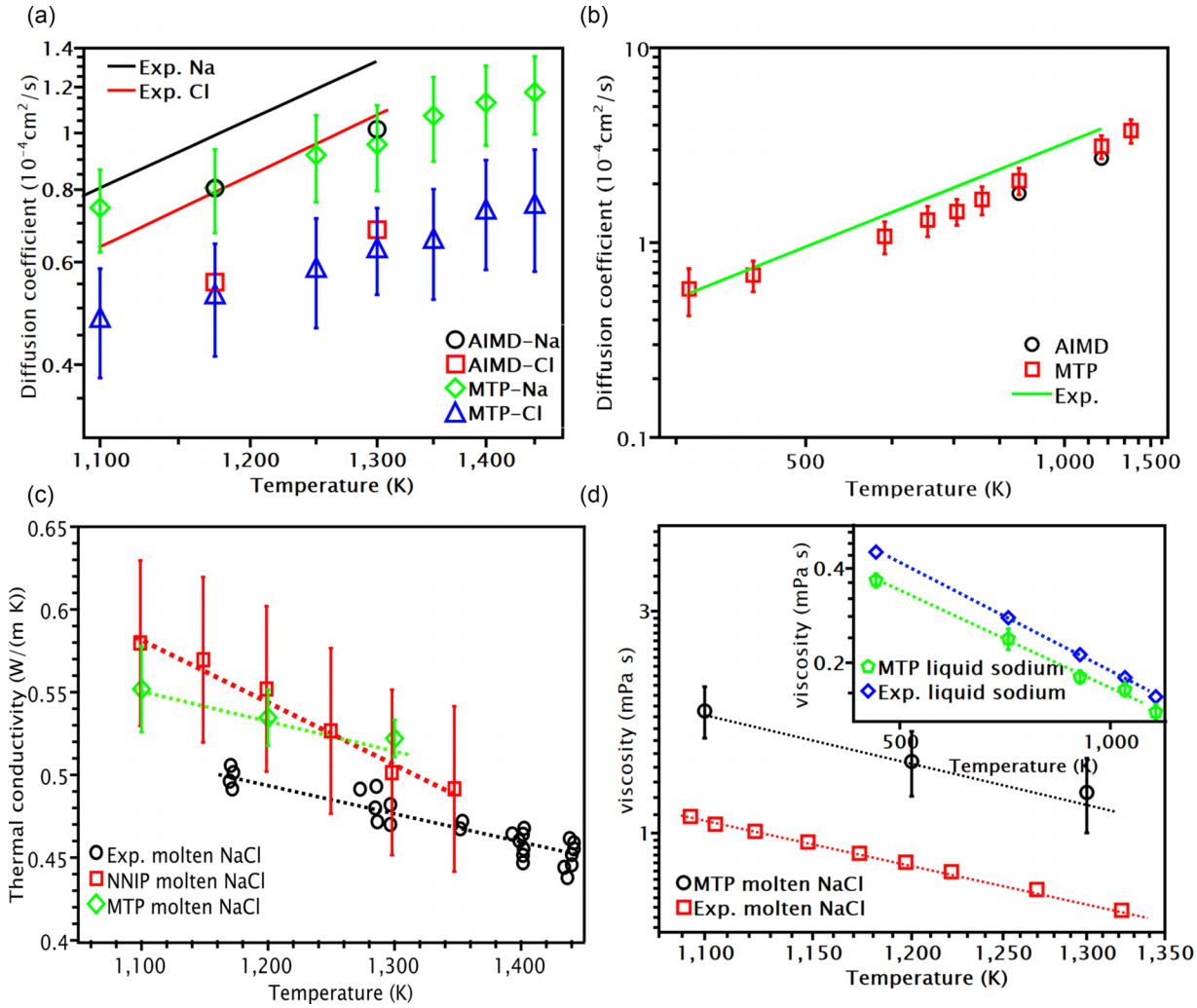

FIG. 3. The prediction of atomic transport properties of molten NaCl and liquid Na. (a) Arrhenius plot of moment tensor potential (MTP)-predicted self-diffusion coefficients of molten NaCl and experimental measured diffusion coefficients [72]. (b) The Arrhenius plot of self-diffusion coefficients of liquid Na and the corresponding experimental values [73]. (c) Comparison of thermal conductivity between our MTP predictions, experimental measurements [74], and molecular dynamics (MD) simulations using neural network interatomic potential (NNIP) [31]. (d) Comparison of viscosity between MTP predictions and experimental measurements [75,76].

stable within a wide range of pressure, yielding the famous ideal gas law $PV = nRT$. Overall, these comparisons confirm that our MTP captures the structural properties of NaCl and Na in both solid and liquid states as well as the covalent bond properties of Cl_2 gas.

C. Atomic transport properties of both liquid Na and molten NaCl

In addition to structures, atomic transport properties and heat capacity are also essential for molten salt selection. Although AIMD can be used to predict ionic self-diffusivity in various binary and ternary salt mixtures [71], MTP-MD allows for larger length and time scales to investigate transport behaviors. Here, we utilized AIMD and MTP-MD to determine the self-diffusion coefficients of different ions from the slope of their mean-squared displacement vs time. Figures 3(a) and 3(b) shows the Arrhenius plots of the self-diffusion coefficients of molten NaCl and liquid Na. The MTP-calculated coefficients are consistent with the AIMD results, on the same order of magnitude (10^{-5} to 10^{-4}cm^2/s) as experimental measurements [72]. Furthermore, Figs. 3(a) and 3(b) show similar slopes for both computational approaches and experimental measurements [72], indicating that MTP also predicts the diffusion activation energies accurately.

Unlike previous work on MD simulations of molten salts that used self-diffusion coefficients to estimate the viscosity [31], we directly evaluated viscosity and thermal conductivity using the reverse nonequilibrium MD method developed by Muller-Plathe [77]. Specifically, we imposed a heat flux by periodically exchanging kinetic energy between two atoms in different regions. The ratio between the kinetic energy exchange rate and the resulting temperature gradient is proportional to the thermal conductivity (see the Supplemental Material [45] for simulation details). Figure 3(c) shows that the MTP predicts thermal conductivities like those obtained using a NNIP [31] and exhibits a temperature dependence

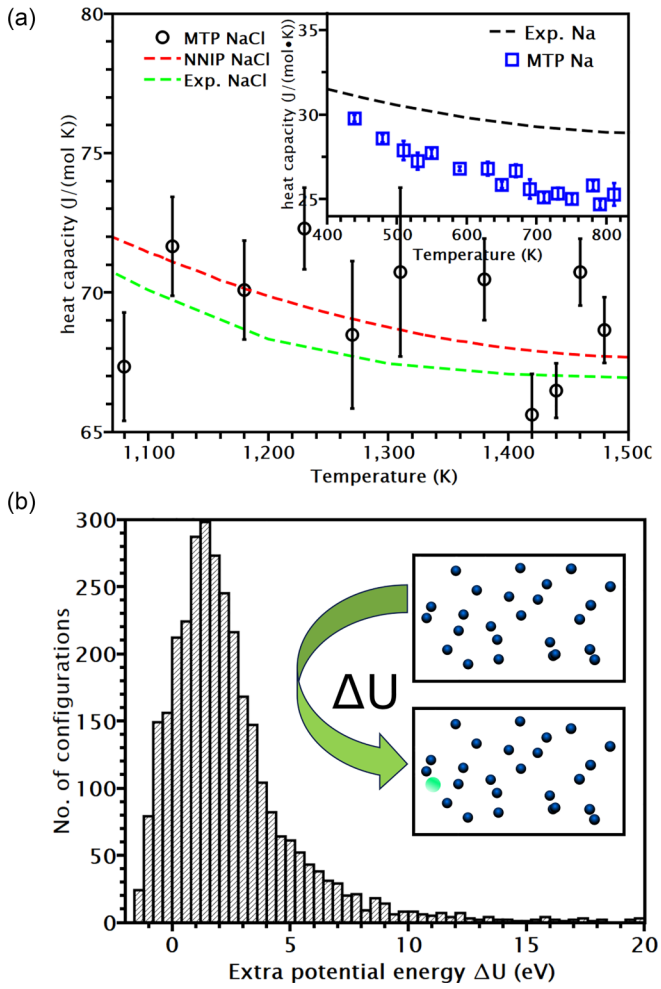

FIG. 4. Prediction of thermodynamic properties of molten NaCl and liquid Na. (a) The assessment of heat capacity predictions of molten NaCl and liquid Na. Error bar represents standard error averaged over 10 samples. Since the melting point of Na is ∼1000 K lower than that of molten NaCl, we plotted the properties of liquid Na at a temperature scale different from that for molten NaCl. (b) The distribution of extra potential energy due to an extra Na atom in an original 117 atom liquid Na model.

closer to experimental results [74]. Likewise, we exchanged the momentum between two atoms in different regions to introduce a momentum flux; the ratio between the momentum flux and the resulting momentum gradient is proportional to viscosity. Because a viscous flow is an activated process obeying the Arrhenius relation [78], we show in Fig. 3(d) an Arrhenius plot of the viscosities obtained with the MTP and values determined experimentally [75,76]. The results predicted by the MTP are in good agreement with experimental measurements, exhibiting similar slopes on the Arrhenius plot and, therefore, similar activation energies.

At last, we calculated the constant-pressure heat capacity of molten NaCl from the enthalpy increase in ∼10 K temperature increment, using a model containing 62 500 atoms under the isothermal-isobaric condition. The MTP predicts a heat capacity of molten NaCl close to both experimental measurements and NNIP predictions [31] [Fig. 4(a)]. Figure 4(a) also shows the heat capacity of liquid Na using the same method. Our MTP predicts approximately the same value and the same downtrend as experimental measurements [79] over a wide temperature range above the melting point. Overall, our MTP predictions match *ab initio* calculations of structural and transport properties of crystalline and molten NaCl, solid and liquid Na, and Cl gas with high accuracy.

D. Calculation of standard reduction potential of Na in molten NaCl

The analysis presented above confirms that the MTP can handle both liquid Na and molten NaCl; here, we focus on the transition of Na from the neutral to the ionic state. This transition is linked to the standard reduction potential of Na, which is proportional to the change in Gibbs free energy ΔG in the redox reaction $\mathrm{Na}(l) + \frac{1}{2}\mathrm{Cl}_2(g) \leftrightharpoons \mathrm{NaCl}(l)$. Here, ΔG can be evaluated as the net change of the chemical potentials μ_g^{ex} between different states along the following pathway:

$$\Delta G = \mu_g^{\mathrm{ex}}(\mathrm{Na}_l \rightarrow \mathrm{Na}_g) + \mu_g^{\mathrm{ex}}(\mathrm{Na}_g \rightarrow \mathrm{Na(NaCl)}_l) - \Delta G_f(\mathrm{Cl}_g^{\bullet}) + \mu_g^{\mathrm{ex}}[\mathrm{Cl}_g \rightarrow \mathrm{Na(NaCl)}_l]. \quad (3)$$

All gaseous states are ideal, so $\Delta G_f(\mathrm{Cl}_g^{\bullet})$ represents the Gibbs free energy of Cl radical gas relative to Cl_2 gas, which is 5.9 kT at 1150 K [61]. Here, μ_g^{ex} of different liquid structures at 1150 K are calculated using the Widom particle insertion method [Fig. 4(b)] [80]: a test particle is inserted randomly (∼800 times) into a configuration of solvent particles (128 atom molten NaCl and 43 atom liquid Na), each time resulting in a distinct potential energy change ΔU. The logarithm of the Boltzmann average of ΔU, $-kT\ln\langle\exp(-\Delta U/kT)\rangle$, gives μ_g^{ex} of the test particle in this solvent. Because DFT gives the ground-state electron distribution, the electron transfers naturally. Trained by DFT results, our MTP can in principle reproduce the effect of charge transfer on total energy.

Following the pathway shown above, we first determined $\mu_g^{\mathrm{ex}}(\mathrm{Na}_l \rightarrow \mathrm{Na}_g)$ using both MTP and DFT. MTP yields approximately the same value (9.58 ± 0.6 kT) as that given by DFT (9.6 ± 0.9 kT). Then the successive transformation of Na and Cl radicals into their ionic states gives μ_g^{ex} of a Na-Cl pair in molten NaCl. The MTP prediction of this value also matches the DFT results (DFT: $-50.1 \pm 4k_BT$; MTP: $-46.8 \pm 3.8k_BT$). Consequently, MTP yields a ΔG (-35.9 ± 4.3 kT) very close to the DFT target (-31.3 ± 4.9 kT). The successful reproduction of the DFT-level ΔG suggests that our MTP can reasonably capture the neutral-to-ionic transition of Na from liquid Na to molten NaCl.

Both DFT and MTP show a negative $\Delta\mu_l$, indicating Na dissolution is favorable. At this concentration level, previous research [81,82] has found that the dissolved Na atoms are ionized and become indistinguishable from other Na ions in the melt. To test whether our MTP distinguishes the dissolved Na from other Na ions, we compared the excess number of Cl neighbors in surplus of Na neighbors (referred to herein as *surplus Cl neighbors*) of solvent Na and dissolved Na within the cutoff distance of our MTP (8Å). Figure 5 shows the number of surplus Cl neighbors for one representative solvent ion and one dissolved Na atom in a 128 atom molten NaCl

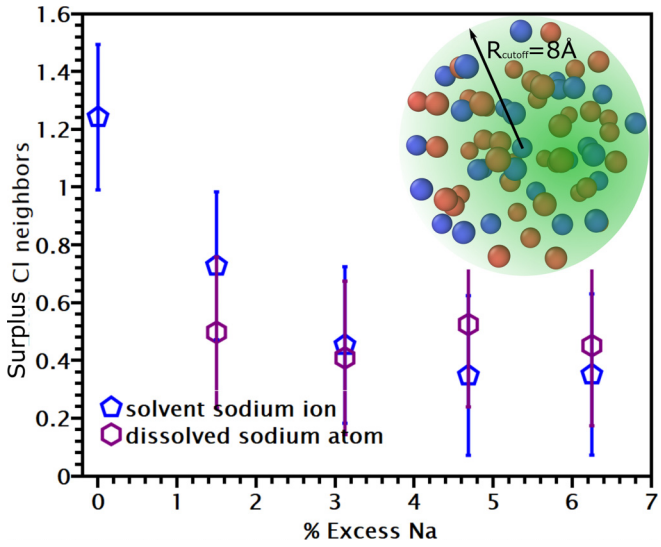

FIG. 5. Change in the number of surplus Cl neighbors of Na upon solvation in NaCl melt.

model, averaging over a 10 ns NVT simulation at 1150 K. The number of surplus Cl neighbors decreases from ∼1.2 in pure NaCl to ∼0.6 when one Na atom is dissolved into the melt. The solvent and dissolved Na atoms have the same amount of surplus Cl neighbors within the error bar, suggesting the same local environment and atomic charge. We also found the dissolved and solvent Na ions have identical atomic energy and Voronoi-cell atomic volume distributions. These findings demonstrate that MTP does treat the dissolved Na atom the same as other Na ions in the melt. The dissolved Na does not perturb the solvent ion network but becomes a part of it, consistent with a previous AIMD study on molten NaCl with dissolved Na [83].

E. Determination of the solubility limit of Na in molten NaCl

Since our MTP captures the neutral-ionic transition of Na, it can be used to determine the solubility limit of Na in molten NaCl. Figure 6(a) illustrates the relative chemical potential $\Delta\mu_l$ upon solvation of Na in molten NaCl at different excess Na concentrations $\mu_g^{\rm ex}[{\rm Na_{extra}(NaCl)}_l;{\rm Na}]-\mu_g^{\rm ex}({\rm Na}_l;{\rm Na})$. Both DFT and MTP show an initial negative $\Delta\mu_l$, indicating Na dissolution is favorable. At this concentration level, the dissolved Na atoms become indistinguishable from other Na ions in the melt [81,82]. $\Delta\mu_l$ becomes positive at ∼3% for MTP, after which Na dissolution is unfavorable. The MTP-predicted solubility limit lies between the DFT prediction and the experimental solubility [84], demonstrating the expressive power of the MTP framework.

Finally, trained by configurations of supersaturated solutions of Na in molten NaCl, our MTP can directly capture the Na partition/dissolution in supersaturated/undersaturated solutions of Na in molten NaCl [Fig. 6(b)]. Starting from a 1 million atom model of molten NaCl, we randomly deleted half of the Cl atoms to create a supersaturated Na solution. On the other hand, we created a void in another 1 million atom model of molten NaCl and filled this void with liquid Na,

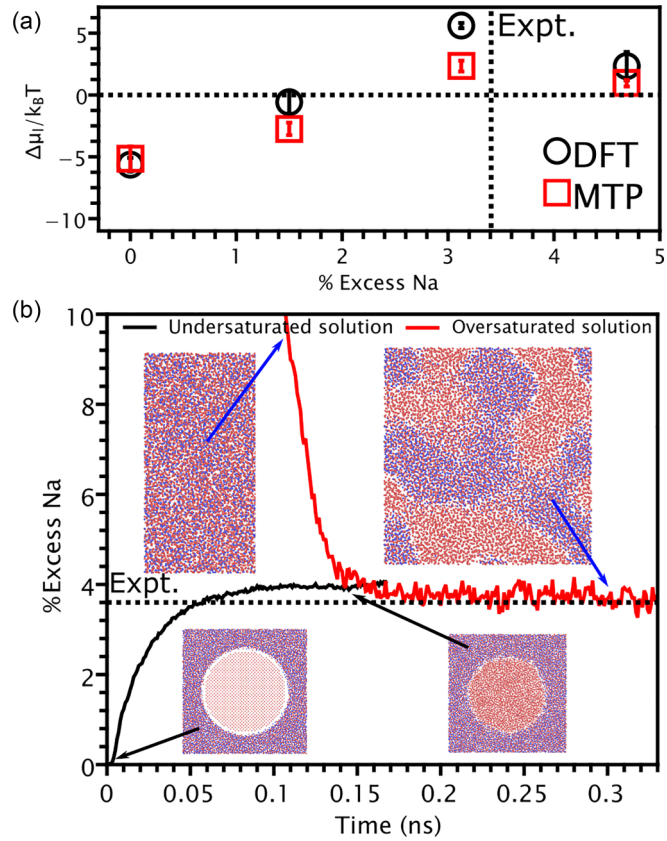

FIG. 6. The determination of solubility limit of Na in molten NaCl. (a) Change in chemical potential of Na upon solvation in NaCl melt upon the molar concentration of excess Na in molten NaCl. The experimental reference is given by the vertical dashed line [84]. (b) The Na partition/dissolution in supersaturated/undersaturated Na solution in molten NaCl at 1150 K.

creating an undersaturated Na solution in contact with liquid Na. During isothermal-isobaric simulation at 1150 K, both models stabilize at the same excess Na concentration close to the experimental solubility limit. These simulations indicate that our MTP can also benefit the material selection of liquid metal/molten salt batteries, which store electrical energy in two liquid metal layers separated by a molten salt electrolyte layer. The primary factor determining the efficiency of such batteries is the metal solubility in molten salt [85,86], for the dissolved metals cause self-discharge currents. The metal solubility in their respective halide melts was found to increase with their atomic number and the atomic number of the halide [87]. Also, the solubility in a molten salt comprising only the cation of the metal is always larger than in a melt containing a plurality of cations. These scientific problems are considered very challenging, and solving them requires fairly aggressive assumptions [87,88]. Our MTP can describe the metal solubility in molten salts with no *a priori* assumption.

IV. DISCUSSION AND CONCLUSIONS

Exploring the mechanisms of metal corrosion in molten salts requires atomic-scale investigations into how salt ions

interact with metal atoms. While MD is well suited for such inquiries, its accuracy is contingent upon the IP employed. This IP must be able to jointly represent salt and metal elements in both ionic and neutral states. Currently, no such IP exists. In response, we developed an MTP to bridge this gap. Our approach features a computationally inexpensive small-cell training dataset, 30% of which are 1 or 2 atom configurations. The resulting MTP can be represented using only a few hundred parameters, yet it empowers IP-MD simulations of complex phenomena which behave very similarly to DFT-MD simulations.

Note that the proposed potential does exhibit limitations, particularly in capturing phonon spectra (see the Supplemental Material [45] for more details). This limitation is likely due to the relatively compact descriptor and simple regressor—linear regression—employed. The potential energy surface describing phonon spectra typically exhibits sharp fluctuations. Our low-level descriptor combined with linear regression is not sufficient to capture such details [89]. However, since our MTP consistently yields reasonable cohesive energies, lattice parameters, bulk moduli, and stable crystalline structures without any imaginary phonon frequencies, all the while involving relatively few parameters and training configurations—i.e., it is computationally efficient both to train and to use—we argue this is a worthwhile trade-off.

Another issue stems from our use of the same DFT setup to calculate the properties of metals, chlorides, and gas. While this consistency simplified the training process, it ignores important corrections that need to be considered to accurately handle gases [90] and ions [91]; these corrections are important to obtain high-quality phase diagrams [91]. As a result, the training errors of previous SNAP [43] or NNIP [31], which were trained only for metals or salts, can be as low as 1 meV/atom. The low training error is partly attributed to the low DFT error of the energy differences among similar structures ($\sim$1 meV/atom [92–94]). However, when assessing the energy difference between different phases, DFT errors can reach dozens of meV/atom [95–97], leading to a higher average error of our MTP ($\sim$7 meV/atom). Given the proof-of-concept nature of this paper, such corrections to different phases were ignored but should be accounted for if such properties must be obtained with high accuracy—in fact, the use of thermodynamic tables for gases, if they are available, are likely a better choice for many calculations. Nonetheless, our MLIP model can reproduce DFT results across multiple phases and yield macroscopic properties in general agreement with experimental measurements. It is a promising tool to help interpret existing molten salt experimental data and predict their properties under conditions without available experimental data.

ACKNOWLEDGMENTS

Financial support for this paper was provided through the Natural Sciences and Engineering Research Council of Canada, Mitacs, and the University Network for Excellence in Nuclear Engineering. We also thank the Digital Research Alliance of Canada (Compute Canada) and the Centre for Advanced Computing at Queen's University for the generous allocation of computer resources. This paper was partly funded by Atomic Energy of Canada Limited, under the auspices of the Federal Nuclear Science and Technology Program.

[1] M. Mehos, C. Turchi, J. Vidal, M. Wagner, Z. Ma, C. Ho, W. Kolb, C. Andraka, and A. Kruizenga, *Concentrating Solar Power Gen3 Demonstration Roadmap* (National Renewable Energy Lab, Golden, 2017).

[2] C.-A. Asselineau, J. Pye, and J. Coventry, Exploring efficiency limits for molten-salt and sodium external cylindrical receivers for third-generation concentrating solar power, Sol. Energy **240**, 354 (2022).

[3] Y. Ge and R. Holze, All-liquid metal battery, Encyclopedia **2**, 1859 (2022).

[4] J. C. Gomez-Vidal and R. Tirawat, Corrosion of alloys in a chloride molten salt (NaCl-LiCl) for solar thermal technologies, Sol. Energy Mater. Sol. Cells **157**, 234 (2016).

[5] R. T. Coyle, T. M. Thomas, and G. Y. Lai, Exploratory corrosion tests on alloys in molten salts at 900 °C, J. Mater. Energy Syst. **7**, 345 (1986).

[6] R. D. Kane, Molten salt corrosion, in *Corrosion: Fundamentals, Testing, and Protection*, edited by S. D. Cramer and B. S. Covino (ASM International, Materials Park, 2003), Vol. 13A, pp. 216–219.

[7] A. Novoselova and V. Smolenski, Electrochemical behavior of neodymium compounds in molten chlorides, Electrochim. Acta **87**, 657 (2013).

[8] L. Feng, C. Guo, and D. Tang, Relationship between the dissolution behaviours and current efficiencies of La, Ce, Pr and Nd in their chloride molten salts, J. Alloys Compd. **234**, 183 (1996).

[9] G. M. Haarberg and J. Thonstad, Electrochemical properties of metal-molten salt mixtures, J. Appl. Electrochem. **19**, 789 (1989).

[10] M. J. L. Sangster and M. Dixon, Interionic potentials in alkali halides and their use in simulations of the molten salts, Adv. Phys. **25**, 247 (1976).

[11] M. Wilson and P. A. Madden, Polarization effects in ionic systems from first principles, J. Phys. Condens. Matter **5**, 2687 (1993).

[12] H. Wang, R. S. DeFever, Y. Zhang, F. Wu, S. Roy, V. S. Bryantsev, C. J. Margulis, and E. J. Maginn, Comparison of fixed charge and polarizable models for predicting the structural, thermodynamic, and transport properties of molten alkali chlorides, J. Chem. Phys. **153**, 214502 (2020).

[13] K. Chenoweth, A. C. T. Van Duin, and W. A. Goddard, ReaxFF reactive force field for molecular dynamics simulations of hydrocarbon oxidation, J. Phys. Chem. A **112**, 1040 (2008).

[14] H. M. Aktulga, J. C. Fogarty, S. A. Pandit, and A. Y. Grama, Parallel reactive molecular dynamics: Numerical methods and algorithmic techniques, Parallel Comput. **38**, 245 (2012).

[15] T. Liang, T.-R. Shan, Y.-T. Cheng, B. D. Devine, M. Noordhoek, Y. Li, Z. Lu, S. R. Phillpot, and S. B. Sinnott, Classical atomistic simulations of surfaces and heterogeneous interfaces with the

charge-optimized many body (COMB) potentials, Mater. Sci. Eng. R Rep. **74**, 255 (2013).

[16] T.-R. Shan, B. D. Devine, T. W. Kemper, S. B. Sinnott, and S. R. Phillpot, Charge-optimized many-body potential for the hafnium/hafnium oxide system, Phys. Rev. B **81**, 125328 (2010).

[17] A. C. T. Van Duin, V. S. Bryantsev, M. S. Diallo, W. A. Goddard, O. Rahaman, D. J. Doren, D. Raymand, and K. Hermansson, Development and validation of a ReaxFF reactive force field for Cu cation/water interactions and copper metal/metal oxide/metal hydroxide condensed phases, J. Phys. Chem. A **114**, 9507 (2010).

[18] S. Cheung, W.-Q. Deng, A. C. T. Van Duin, and W. A. Goddard, $\mathrm{ReaxFF_{MgH}}$ reactive force field for magnesium hydride systems, J. Phys. Chem. A **109**, 851 (2005).

[19] L. Liu, Y. Liu, S. V. Zybin, H. Sun, and W. A. Goddard, ReaxFF$-lg$: Correction of the ReaxFF reactive force field for London dispersion, with applications to the equations of state for energetic materials, J. Phys. Chem. A **115**, 11016 (2011).

[20] J. Guo, L. Ward, Y. Babuji, N. Hoyt, M. Williamson, I. Foster, N. Jackson, C. Benmore, and G. Sivaraman,Composition-transferable machine learning potential for LiCl-KCl molten salts validated by high-energy x-ray diffraction, Phys. Rev. B **106**, 014209 (2022).

[21] J. Guo, V. Woo, D. A. Andersson, N. Hoyt, M. Williamson, I. Foster, C. Benmore, N. E. Jackson, and G. Sivaraman, AL4GAP: Active learning workflow for generating DFT-SCAN accurate machine-learning potentials for combinatorial molten salt mixtures, J. Chem. Phys. **159**, 024802 (2023).

[22] G. Sivaraman, J. Guo, L. Ward, N. Hoyt, M. Williamson, I. Foster, C. Benmore, and N. Jackson, Automated development of molten salt machine learning potentials: Application to LiCl, J. Phys. Chem. Lett. **12**, 4278 (2021).

[23] J. Behler and M. Parrinello, Generalized neural-network representation of high-dimensional potential-energy surfaces, Phys. Rev. Lett. **98**, 146401 (2007).

[24] A. P. Bartók, M. C. Payne, R. Kondor, and G. Csányi, Gaussian approximation potentials: The accuracy of quantum mechanics, without the electrons, Phys. Rev. Lett. **104**, 136403 (2010).

[25] N. Artrith, T. Morawietz, and J. Behler, High-dimensional neural-network potentials for multicomponent systems: Applications to zinc oxide, Phys. Rev. B **83**, 153101 (2011).

[26] J. S. Smith, O. Isayev, and A. E. Roitberg, ANI-1: An extensible neural network potential with DFT accuracy at force field computational cost, Chem. Sci. **8**, 3192 (2017).

[27] B. Onat, E. D. Cubuk, B. D. Malone, and E. Kaxiras, Implanted neural network potentials: Application to Li-Si alloys, Phys. Rev. B **97**, 094106 (2018).

[28] G. P. P. Pun, R. Batra, R. Ramprasad, and Y. Mishin, Physically informed artificial neural networks for atomistic modeling of materials, Nat. Commun. **10**, 2339 (2019).

[29] S.-C. Lee, Y. Zhai, Z. Li, N. P. Walter, M. Rose, B. J. Heuser, and Z. Y., Comparative studies of the structural and transport properties of molten salt FLiNaK using the machine-learned neural network and reparametrized classical forcefields, J. Phys. Chem. B **125**, 10562 (2021).

[30] S. T. Lam, Q.-J. Li, R. Ballinger, C. Forsberg, and J. Li, Modeling LiF and FLiBe molten salts with robust neural network interatomic potential, ACS Appl. Mater. Interfaces **13**, 24582 (2021).

[31] Q.-J. Li, E. Küçükbenli, S. Lam, B. Khaykovich, E. Kaxiras, and J. Li, Development of robust neural-network interatomic potential for molten salt, Cell Rep. Phys. Sci. **2**, 100359 (2021).

[32] T. Xu, X. Li, Y. Wang, and Z. Tang, Development of deep potentials of molten $MgCl_2$-NaCl and $MgCl_2$-KCl salts driven by machine learning, ACS Appl. Mater. Interfaces **15**, 14184 (2023).

[33] T. W. Ko, J. A. Finkler, S. Goedecker, and J. Behler, A fourth-generation high-dimensional neural network potential with accurate electrostatics including non-local charge transfer, Nat. Commun. **12**, 398 (2021).

[34] A. Mondal, D. Kussainova, S. Yue, and A. Z. Panagiotopoulos, Modeling chemical reactions in alkali carbonate-hydroxide electrolytes with deep learning potentials, J. Chem. Theory Comput. **19**, 4584 (2023).

[35] R. Chahal, S. Roy, M. Brehm, S. Banerjee, V. Bryantsev, and S. T. Lam, Transferable deep learning potential reveals intermediate-range ordering effects in LiF-NaF-ZrF_4 molten salt, JACS Au **2**, 2693 (2022).

[36] I. S. Novikov, K. Gubaev, E. V. Podryabinkin, and A. V. Shapeev, The MLIP package: Moment tensor potentials with MPI and active learning, Mach. Learn. Sci. Technol. **2**, 025002 (2021).

[37] A. V. Shapeev, Moment tensor potentials: A class of systematically improvable interatomic potentials, Multiscale Model. Simul. **14**, 1153 (2016).

[38] E. Podryabinkin, K. Garifullin, A. Shapeev, and I. Novikov, MLIP-3: Active learning on atomic environments with moment tensor potentials, J. Chem. Phys. **159**, 084112 (2023).

[39] J. Qi, S. Banerjee, Y. Zuo, C. Chen, Z. Zhu, M. L. Holekevi Chandrappa, X. Li, and S. P. Ong, Bridging the gap between simulated and experimental ionic conductivities in lithium superionic conductors, Mater. Today Phys. **21**, 100463 (2021).

[40] X.-G. Li, C. Chen, H. Zheng, Y. Zuo, and S. P. Ong, Complex strengthening mechanisms in the NbMoTaW multi-principal element alloy, Npj Comput. Mater. **6**, 70 (2020).

[41] Z. Deng, C. Chen, X.-G. Li, and S. P. Ong, An electrostatic spectral neighbor analysis potential for lithium nitride, Npj Comput. Mater. **5**, 75 (2019).

[42] Y. Zuo, C. Chen, X. Li, Z. Deng, Y. Chen, J. Behler, G. Csányi, A. V. Shapeev, A. P. Thompson, M. A. Wood *et al.*, Performance and cost assessment of machine learning interatomic potentials, J. Phys. Chem. A **124**, 731 (2020).

[43] X.-G. Li, C. Hu, C. Chen, Z. Deng, J. Luo, and S. P. Ong, Quantum-accurate spectral neighbor analysis potential models for Ni-Mo binary alloys and fcc metals, Phys. Rev. B **98**, 094104 (2018).

[44] D. Guo, J. Zhao, W. Liang, and G. Lu, Molecular dynamics simulation of molten strontium chloride based on deep potential, J. Mol. Liq. **348**, 118380 (2022).

[45] See Supplemental Material at http://link.aps.org/supplemental/10.1103/PhysRevB.109.174113 for (brief description).

[46] P. Giannozzi, S. Baroni, N. Bonini, M. Calandra, R. Car, C. Cavazzoni, D. Ceresoli, G. L. Chiarotti, M. Cococcioni, I. Dabo *et al.*, QUANTUM ESPRESSO: A modular and open-source software project for quantum simulations of materials, J. Phys. Condens. Matter **21**, 395502 (2009).

[47] J. P. Perdew, K. Burke, and M. Ernzerhof, Generalized gradient approximation made simple, Phys. Rev. Lett. **77**, 3865 (1996).

[48] B. Delley, Hardness conserving semilocal pseudopotentials, Phys. Rev. B **66**, 155125 (2002).

[49] M. Liu, P. Masset, and A. Gray-Weale, Solubility of sodium in sodium chloride: A density functional theory molecular dynamics study, J. Electrochem. Soc. **161**, E3042 (2014).

[50] S. Grimme, Semiempirical GGA-type density functional constructed with a long-range dispersion correction, J. Comput. Chem. **27**, 1787 (2006).

[51] H. J. C. Berendsen, J. P. M. Postma, W. F. Van Gunsteren, A. DiNola, and J. R. Haak, Molecular dynamics with coupling to an external bath, J. Chem. Phys. **81**, 3684 (1984).

[52] W. G. Hoover, Canonical dynamics: Equilibrium phase-space distributions, Phys. Rev. A **31**, 1695 (1985).

[53] N. Grønbech-Jensen, Complete set of stochastic Verlet-type thermostats for correct Langevin simulations, Mol. Phys. **118**, e1662506 (2020).

[54] A. A. Mamun, S. Xu, X.-G. Li, and Y. Su, Comparing interatomic potentials in calculating basic structural parameters and Peierls stress in tungsten-based random binary alloys, Phys. Scr. **98**, 105923 (2023).

[55] F. G. Fumi and M. P. Tosi, Ionic sizes and born repulsive parameters in the NaCl-type alkali halides—I, J. Phys. Chem. Solids **25**, 31 (1964).

[56] Y. Luo, J. A. Meziere, G. D. Samolyuk, G. L. W. Hart, M. R. Daymond, and L. K. Béland, A set of moment tensor potentials for zirconium with increasing complexity, J. Chem. Theory Comput. **19**, 6848 (2023).

[57] J. A. Meziere, Y. Luo, Y. Xia, L. K. Béland, M. R. Daymond, and G. L. W. Hart, Accelerating training of MLIPs through small-cell training, J. Mater. Res. **38**, 5095 (2023).

[58] A. M. Miksch, T. Morawietz, J. Kästner, A. Urban, and N. Artrith, Strategies for the construction of machine-learning potentials for accurate and efficient atomic-scale simulations, Mach. Learn. Sci. Technol. **2**, 031001 (2021).

[59] W. T. Barrett and W. E. Wallace, Studies of NaCl-KCl solid solutions. I. Heats of formation, lattice spacings, densities, Schottky defects and mutual solubilities, J. Am. Chem. Soc. **76**, 366 (1954).

[60] A. M. Halpern, From dimer to crystal: Calculating the cohesive energy of rare gas solids, J. Chem. Educ. **89**, 592 (2012).

[61] M. W. Chase, NIST-JANAF thermochemical tables for the bromine oxides, J. Phys. Chem. Ref. Data **25**, 1069 (1996).

[62] *Handbook of Chemistry and Physics: A Ready-Reference Book of Chemical and Physical Data*, edited by R. C. Weast (CRC Press, Boca Raton, 1984).

[63] L. M. Thomas and J. Shanker, Equations of state and pressure dependence of bulk modulus for NaCl crystals, Phys. Status Solidi B **189**, 363 (1995).

[64] F. Cardarelli, Less common nonferrous metals, in *Materials Handbook* (Springer, London, 2008), pp. 213–454.

[65] R. W. Dreyfus and A. S. Nowick, Energy and entropy of formation and motion of vacancies in NaCl and KCl crystals, J. Appl. Phys. **33**, 473 (1962).

[66] G. Jacucci and R. Taylor, The calculation of vacancy formation energies in the alkali metals Li, Na and K, J. Phys. F Met. Phys. **9**, 1489 (1979).

[67] G. J. Janz, Thermodynamic and transport properties for molten salts: Correlation equations for critically evaluated density, surface tension, electrical conductance, and viscosity data, J. Phys. Chem. Ref. Data **17**, 311 (1988).

[68] F. G. Edwards, J. E. Enderby, R. A. Howe, and D. I. Page, The structure of molten sodium chloride, J. Phys. C: Solid State Phys. **8**, 3483 (1975).

[69] S. Biggin and J. E. Enderby, Comments on the structure of molten salts, J. Phys. C: Solid State Phys. **15**, L305 (1982).

[70] S. Grimme, J. Antony, S. Ehrlich, and H. Krieg, A consistent and accurate *ab initio* parametrization of density functional dispersion correction (DFT-D) for the 94 elements H-Pu, J. Chem. Phys. **132**, 154104 (2010).

[71] S. T. Lam, Q.-J. Li, J. Mailoa, C. Forsberg, R. Ballinger, and J. Li, The impact of hydrogen valence on its bonding and transport in molten fluoride salts, J. Mater. Chem. A **9**, 1784 (2021).

[72] G. J. Janz and N. P. Bansal, Molten salts data: Diffusion coefficients in single and multi-component salt systems, J. Phys. Chem. Ref. Data **11**, 505 (1982).

[73] R. E. Meyer and N. H. Nachtrieb, Self-diffusion of liquid sodium, J. Chem. Phys. **23**, 1851 (1955).

[74] Y. Nagasaka, N. Nakazawa, and A. Nagashima, Experimental determination of the thermal diffusivity of molten alkali halides by the forced Rayleigh scattering method. I. Molten LiCl, NaCl, KCl, RbCl, and CsCl, Int. J. Thermophys. **13**, 555 (1992).

[75] T. Ito, N. Kojima, and A. Nagashima, Redetermination of the viscosity of molten NaCl at elevated temperatures, Int. J. Thermophys. **10**, 819 (1989).

[76] A. V. Grosse, Viscosities of liquid sodium and potassium, from their melting points to their critical points, Science **147**, 1438 (1965).

[77] F. Müller-Plathe, A simple nonequilibrium molecular dynamics method for calculating the thermal conductivity, J. Chem. Phys. **106**, 6082 (1997).

[78] D. Zhao, L. Yan, T. Jiang, S. Peng, and B. Yue, On the viscosity of molten salts and molten salt mixtures and its temperature dependence, J. Energy Storage **61**, 106707 (2023).

[79] J. K. Fink and L. Leibowitz, *Thermodynamic and Transport Properties of Sodium Liquid and Vapor* (Argonne National Laboratory, Argonne, 1995).

[80] B. Widom, Some topics in the theory of fluids, J. Chem. Phys. **39**, 2808 (1963).

[81] H. H. Kristoffersen and H. Metiu, Chemistry of solvated electrons in molten alkali chloride salts, J. Phys. Chem. C **122**, 19603 (2018).

[82] P. Pegolo, S. Baroni, and F. Grasselli, Self-interaction and transport of solvated electrons in molten salts, J. Chem. Phys. **159**, 094116 (2023).

[83] S. Roy, Y. Liu, M. Topsakal, E. Dias, R. Gakhar, W. C. Phillips, J. F. Wishart, D. Leshchev, P. Halstenberg, S. Dai *et al.*, A holistic approach for elucidating local structure, dynamics, and speciation in molten salts with high structural disorder, J. Am. Chem. Soc. **143**, 15298 (2021).

[84] M. A. Bredig and H. R. Bronstein, Miscibility of liquid metals with salts. IV. The sodium-sodium halide systems at high temperatures, J. Phys. Chem. **64**, 64 (1960).

[85] H. Kim, D. A. Boysen, J. M. Newhouse, B. L. Spatocco, B. Chung, P. J. Burke, D. J. Bradwell, K. Jiang, A. A. Tomaszowska, K. Wang *et al.*, Liquid metal batteries: Past, present, and future, Chem. Rev. **113**, 2075 (2013).

[86] Y. Ding, X. Guo, Y. Qian, L. Xue, A. Dolocan, and G. Yu, Room-temperature all-liquid-metal batteries based on fusible

alloys with regulated interfacial chemistry and wetting, Adv. Mater. **32**, 2002577 (2020).

[87] M. A. Bredig, *Mixtures of Metals with Molten Salts* (Oak Ridge National Laboratory, Oak Ridge, 1963).

[88] E. A. Ukshe and N. G. Bukun, The dissolution of metals in fused halides, Russ. Chem. Rev. **30**, 90 (1961).

[89] Y. Liu, X. He, and Y. Mo, Discrepancies and error evaluation metrics for machine learning interatomic potentials, npj Comput. Mater. **9**, 174 (2023).

[90] E. Sargeant, F. Illas, P. Rodríguez, and F. Calle-Vallejo, Importance of the gas-phase error correction for O_2 when using DFT to model the oxygen reduction and evolution reactions, J. Electroanal. Chem. **896**, 115178 (2021).

[91] F. Jensen, Describing anions by density functional theory: Fractional electron affinity, J. Chem. Theory Comput. **6**, 2726 (2010).

[92] S. Kharabadze, A. Thorn, E. A. Koulakova, and A. N. Kolmogorov, Prediction of stable Li-Sn compounds: Boosting *ab initio* searches with neural network potentials, npj Comput. Mater. **8**, 136 (2022).

[93] A. N. Kolmogorov and V. H. Crespi, Registry-dependent interlayer potential for graphitic systems, Phys. Rev. B **71**, 235415 (2005).

[94] W. Ibarra-Hernández, S. Hajinazar, G. Avendaño-Franco, A. Bautista-Hernández, A. N. Kolmogorov, and A. H. Romero, Structural search for stable Mg-Ca alloys accelerated with a neural network interatomic model, Phys. Chem. Chem. Phys. **20**, 27545 (2018).

[95] A. M. De Andrade, J. Kullgren, and P. Broqvist, Improving the transferability of density functional theory predictions through correlation analysis: Structural and energetic properties of Ni X alloys (X = C, Si, Ge, and Sn), Phys. Rev. B **105**, 085127 (2022).

[96] L. Wang, T. Maxisch, and G. Ceder, Oxidation energies of transition metal oxides within the GGA + U framework, Phys. Rev. B **73**, 195107 (2006).

[97] A. N. Kolmogorov, S. Shah, E. R. Margine, A. F. Bialon, T. Hammerschmidt, and R. Drautz, New superconducting and semiconducting Fe-B compounds predicted with an *ab initio* evolutionary search, Phys. Rev. Lett. **105**, 217003 (2010).